

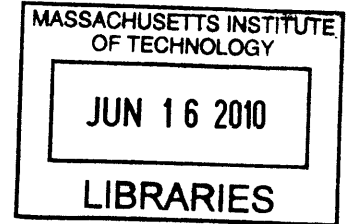
Photonic Bandgap Fibers for Transmitting High Peak-Power
Pulses in the Near Infrared

by

Zachary Ruff

A.B. Engineering Science, 2004
Dartmouth College

B.E. Engineering Science, 2005
Thayer School of Engineering at Dartmouth College



ARCHIVES

Submitted to the Department of Materials Science and Engineering
in Partial Fulfillment of the Requirements for the Degree of

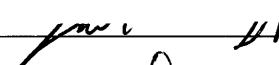
Masters of Science in Materials Science and Engineering
at the Massachusetts Institute of Technology

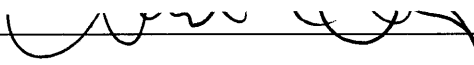
June 2010

©2010 Massachusetts Institute of Technology
All rights reserved

Signature of Author: _____

Department of Materials Science and Engineering
April, 8th 2010

Certified by: _____

Thomas B. King Associate Professor of Materials Science
Thesis Supervisor

Accepted by: _____

Christine Ortiz
Associate Professor of Materials Science
Chair, Departmental Committee on Graduate Students

Photonic Bandgap Fibers for Transmitting High Peak-Power Pulses in the Near Infrared

by

Zachary Ruff

Submitted to the Department of Materials Science and Engineering
on April 8th, 2010 in Partial Fulfillment of the Requirements for the Degree of
Masters of Science in Materials Science and Engineering

ABSTRACT: Hollow-core photonic bandgap fibers (PBG) offer the opportunity to suppress highly the optical absorption and nonlinearities of their constituent materials, which makes them viable candidates for transmitting high-peak power pulses. This thesis demonstrates the fabrication and characterization of polymer-composite PBG fibers in a novel materials system, polycarbonate and arsenic sulfide glass. Propagation losses for the 60 μm -core fibers are less than 2dB/m, a 52x improvement over previous PBG fibers at this wavelength. Through preferential coupling the fiber is capable of operating with over 97% the fiber's power output in the fundamental (HE_{11}) mode. The fiber transmitted pulses with peak powers of 11.4 MW before failure.

Thesis Supervisor: Yoel Fink

Title: Thomas B. King Associate Professor of Materials Science

Acknowledgements:

I would like to thank my advisor Yoel Fink, who has been my teacher and mentor throughout my graduate studies. His vision and hard work have been inspirational and it has been under his guidance that this thesis work has been achieved. I would also like to thank all of the members of his research group at MIT, the Photonic Bandgap Fiber and Devices Group, with whom I have collaborated with over the years: Ayman Abouraddy, Mehmet Bayindir, Gilles Benoit, Noemi Chocat, Sylvain Danto, Daosheng Deng, Shunji Egusa, Ken Kuriki, Ofer Shapira, Nick Orf, Peter Rakich, Dana Shemuly, Fabien Sorin, Sasha Stolyorav, Jeff Viens, and Zheng Wang. Before studying photonic bandgap fibers, I worked with Peter Rakich for two years researching non-linear optics in chalcogenide fibers, and although this work does not appear in this thesis, the expertise I developed working with Peter was vital to the completion of this thesis. Over the last two years, I have worked most closely with Dana Shemuly, whose contributions can be seen throughout this work.

Finally, I would like to thank all of my family and friends, who have supported me throughout this work, especially my parents Myra and Roy Ruff.

Table of Contents

I	INTRODUCTION AND BACKGROUND	5
I.A	Introduction.....	5
I.B	High-Peak Power Laser Pulses	6
I.C	Photonic Bandgap Fibers.....	7
II	MATERIALS SELECTION AND ANALYSIS.....	10
II.A	Polymer.....	10
II.B	Chalcogenide Glass.....	11
II.C	Optical Constants	14
III	FIBER FABRICATION	17
III.A	Glass Synthesis.....	17
III.B	Film deposition.....	18
III.C	Preform fabrication.....	20
III.D	Fiber Drawing: Optimizing Draw Parameters	22
III.D.1	Controlling the Fiber's Outer Diameter and Stress	23
III.D.2	Controlling the NS Ratio.....	26
III.D.3	Monitoring the Photonic Bandgap.....	27
IV	FIBER ANALYSIS AND TRANSMISSION MEASUREMENTS.....	31
IV.A	Draw Slides and Pre-Screening Fibers	31
IV.B	Fiber Cross-sectional Images and Analysis	32
IV.C	Propagation Loss Measurements	33
IV.D	Modal Analysis	35
IV.E	Power Handling Measurements	36
V	CONCLUSION AND FUTURE DIRECTIONS	38
VI	APPENDIX: END-FACET PREPARATION	39
VII	REFERENCES.....	41

I Introduction and Background

I.A Introduction

Fiber optics have inherently long interaction lengths that make them model devices for guiding and manipulating light. The continuous nature of the fiber drawing technique allows for fibers to be fabricated uniformly on the kilometer length scale, leading to relatively inexpensive devices. As a result, fiber optics have become ubiquitous, often becoming the dominant technology for many communications, military, industrial and medical applications.

First demonstrated only ten years ago, one-dimensional photonic bandgap fibers (PBG) are a comparatively new technology with respect to the step-index silica fibers. PBG fibers guide light using a fundamentally different physical mechanism, relying on the coherent reflection of light rather than total internal reflection. These coherent reflections occur when light interacts with a periodic structure of high-index contrast layers forming a dielectric mirror, through which a given set of wavelengths cannot propagate.

Previous investigations have demonstrated some of the unique properties and potential uses of PBG fibers [6-12]. High-index contrast structures demonstrate omnidirectional reflectivity [7] and can be incorporated into optical fibers by co-drawing a low-index polymer with a high-index chalcogenide glass [8]. By simply scaling the dimensions of the bi-layer structures, the co-drawing technique has been used to draw fibers that transmit light from less than $1\mu\text{m}$ out past $10\mu\text{m}$, suppressing the relatively high absorption losses of the constituent materials [9,10]. Cavities can also be introduced

into the fibers in order to tailor dispersion for applications such as dispersion compensation and pulse compression [11].

Earlier works in our research group demonstrated the feasibility of using PBG fibers for transmitting NIR radiation. These fibers had relatively large core-sizes and high transmission losses, making their analysis challenging. In this thesis, a new materials system is introduced in which to fabricate PBG fibers with reduced core sizes. This development has allowed for the fabrication of fibers with modal content approaching step-index silica fibers and transmission losses practical for many applications of high-peak power laser pulses.

1.B High-Peak Power Laser Pulses

High-peak power laser pulses in the near infrared (NIR) have important medical, industrial and military applications. In conventional single-mode silica fibers, the damage threshold due to the core material's finite optical absorption, and the pulse distortion induced by the core material's self-phase modulation limit the transmitted peak power. To reduce the optical power density in the core, large mode-area silica fibers have been developed, but poor-mode quality, peak-power limitations and coupling instabilities limit their suitability for many applications [1].

An alternative approach is to guide the pulse using either a mirror or a photonic bandgap, eliminating the core material. Large-core hollow fibers such as polymer-metal waveguides have been shown to transmit high-peak power pulses, but poor mode quality too restricts their performance [2]. Air-silica 2D-photonic crystal fibers (PCF) can deliver pulses without compromising mode-quality, though they can have a somewhat limited damage threshold, since even commercially optimized designs confine only

~98% of the transmitted power to the air-core of the fiber [3,4]. In this thesis, we will show that 1D-PCF or photonic bandgap (PBG) fibers can strongly confine light to a hollow core, suppressing materials absorption and nonlinearities by over 5 orders of magnitude, while still delivering mode qualities approaching that of a step-index single mode fiber [5].

I.C Photonic Bandgap Fibers

In order to understand the light guiding mechanism of PBG fibers, it is helpful to first consider a planar multilayer film with infinite periodic layers of alternating materials with different refractive indices. When monochromatic light with a wavelength λ_0 and an angle of incidence θ , hits the film there will be a set of wavelengths and angles of incidence for which the light will be strongly reflected due to the Bragg condition. This condition is satisfied when the incident light experiences a π -phase shift over a period of layers or bilayers, causing the light to be reflected coherently at each interface.

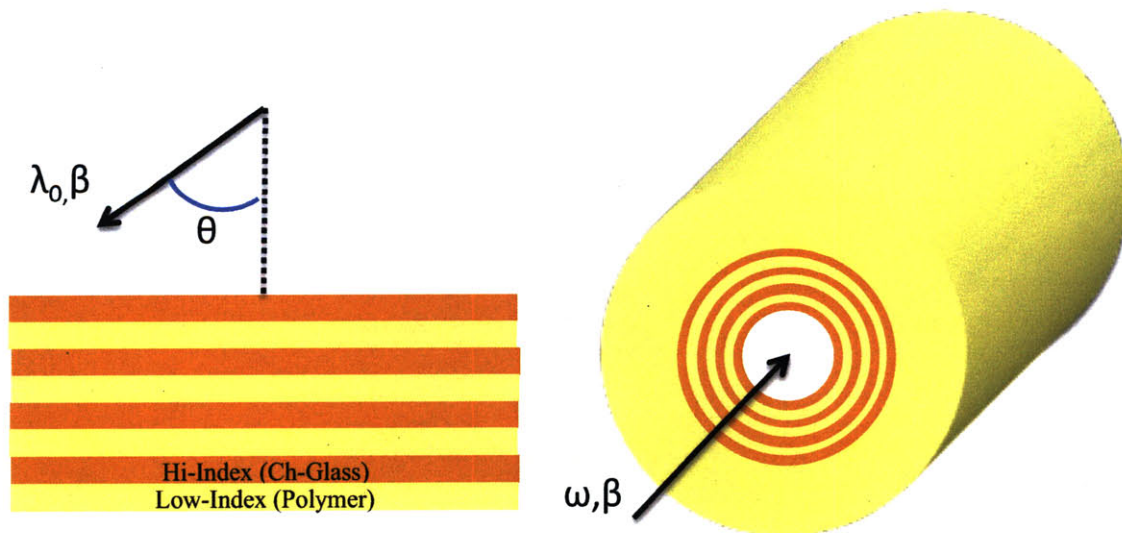


Figure 1: Schematics of a PBG multilayer film (left) and PBG fiber (right)

At normal incidence ($\theta=0$) to the film, plane waves with the transverse electric (TE) and transverse magnetic (TM) polarizations behave identically. Away from normal incidence the degeneracy is broken and it then becomes necessary to decompose the light into its two orthogonal polarizations. Since the multilayer film is invariant in the plane of the film, the polarization, frequency and angle of incidence completely describes the incident light [21]. By defining an appropriate reflectivity cut-off, the band structure of the mirror can then be calculated using the transfer-matrix method [6] and plotted for λ_0 , θ or more commonly ω , β (the axial wave-vector) pairs. The plot can be divided into regions or bands where light can propagate through the film and regions where it will be strongly reflected called bandgaps. It can be shown that both the width and the magnitude of the bandgaps will be maximized for layer thicknesses (d) that satisfy the quarter-wavelength condition,

$$\frac{\lambda}{4} = d_{low} n_{low} = d_{high} n_{high} \text{ at normal incidence } (\beta=0) \text{ and}$$

$$\frac{\lambda}{4} = d_{low} \sqrt{n_{low}^2 - 1} = d_{high} \sqrt{n_{high}^2 - 1} \text{ at grazing incidence } (\beta \sim w/c).$$

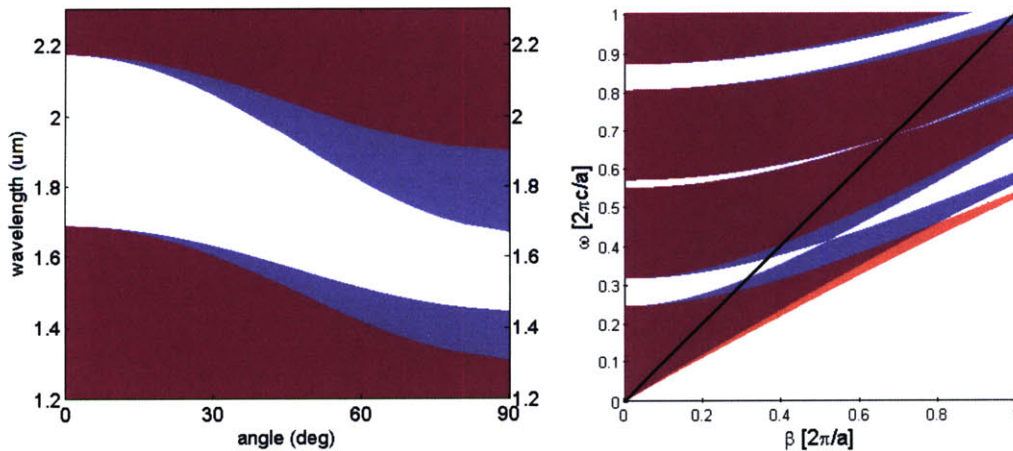


Figure 2: Simulated band diagram for an ideal PBG structure of $As_{25}S_{75}$ and polycarbonate with a fundamental bandgap centered at $1.55\mu m$ plotted as a function of λ , θ pairs (left) and ω , β pairs (right). Regions with propagating modes are shaded (blue for TM, red for TE and purple for both).

At the limit where the core-size is much larger than the bilayer thickness, the band-structure of a planar film is a good approximation for a cylindrical fiber. Under this condition, a PBG fiber will support a number of modes. The modes of interest for transmitting light in PBG fiber will be at grazing incidence, where the modes closest to the light line ($\beta \sim \omega/c$, $\theta \sim 90$). A detailed analysis of the fiber's mode structure can be found in the literature and is out of the scope of this thesis [5,23]. For this work, it is sufficient to recognize that the number of modes PBG fibers support scales strongly with the fiber's core diameter and that the spacing between these modes scales as $1/R_{\text{core}}^2$ [5].

PBG fibers have two competing fiber contributions to their propagation losses, materials losses and inter-modal coupling [21]. The bulk materials losses, such as materials absorption and bulk scattering, are due to finite penetration of the light's electric field into the PBG structure. These losses have been shown to scale as $1/R_{\text{core}}^3$, which takes into account both the geometry of the system and the amplitude of the electric field [5,21]. Certainly, increasing the fiber's core size will decrease materials losses, but as fiber's core size gets larger, the spacing between modes decreases, facilitating intermodal coupling. Since higher-order modes interact more strongly with the PBG, this mechanism leads to an overall increase in propagation losses. Therefore, the core-size must be optimized to mitigate the contributions of both materials losses and intermodal coupling.

II Materials Selection and Analysis

The co-drawing technique for PBG fibers requires two component amorphous materials to form the periodic dielectric structure, a high and low index material. In this thesis, the discussion will be restricted to using a thermoplastic polymer as the low-index material and a chalcogenide glass as the high-index material. However, in practice any combination of amorphous materials with similar thermal visco-elastic properties could be used.

II.A Polymer

Previous investigations into polymer-composite fibers used high temperature thermoplastics, such as polyethersulfone (PES) and polyetherimide (PEI) that have relatively high extinction coefficients compared to more common optical polymers. In this work, we demonstrate that optical polymers with lower extinction coefficients can be used to further reduce the absorption losses of PBG fibers. We chose polycarbonate over other amorphous optical polymers, such as cyclic-olefins, due to its commercial availability at experimentally favorable film thicknesses.

The commercial availability of thin polymer films is critical for the fabrication of PBG fibers. A PBG optimized to satisfy the quarter-wavelength condition at 1.55 microns requires polymer layer thicknesses of around 300 nanometers. The geometric constraints of the draw process limit the draw ratio, the ratio of the outer diameter of the preform to the outer diameter of the fiber, to around 100, driving the need for polymer film thicknesses less than 30 μ m. Currently, few optical polymers can be either extruded or solvent cast with an acceptable tolerance at these film thicknesses.

Polycarbonate's extinction coefficient at 1.55 μm is over an order of magnitude less than either PES's or PEI's coefficient, pushing the absorption loss limit for PBG fibers below 0.05 dB/m for a 60 μm core fiber. Polycarbonate also exhibits low absorption into the visible spectrum, creating the opportunity for low-loss fibers with bandgaps approaching ultra-violet wavelengths. For this work, we were able only to source films extruded from a general use polycarbonate resin (Lexan 104), which contained significant inclusions (dust, poor molecular weight distribution). We expect an optical grade film to further improve transmission losses.

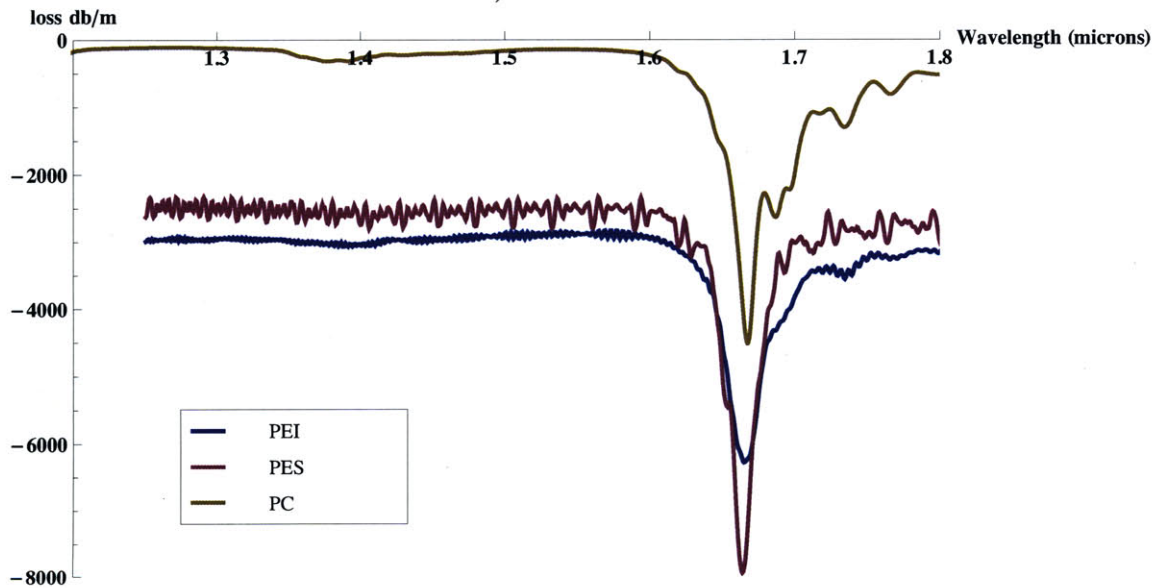


Figure 3: Plot of the extinction coefficients of polymers measured using a Fourier transform infrared spectrometer. The oscillations seen in the PEI and PES measurements are due to the Fabry-Perot cavity formed in thin samples. The absorption coefficient of polycarbonate is less than 150 dB/m at 1550nm.

II.B Chalcogenide Glass

The melt-quench technique (described in section III.A) is a powerful technique for synthesizing chalcogenide glasses in a wide variety of compositions. Many chalcogenide glasses have robust glass forming regions that allow these materials to be

engineered to take on a range of physical properties. As a result, it is often possible to tune independently the optical and thermo-mechanical properties for a given application. For this work, we have selected the arsenic-sulfide glass system due to its low optical absorption in the NIR. The robust glass formation window in this system also allows for the glass's composition to be tuned to co-draw with polycarbonate. A literature search suggested that a composition with a relatively high sulfur atomic percent ($\text{As}_{25}\text{S}_{75}$) would be an appropriate starting point for experimentation [14].

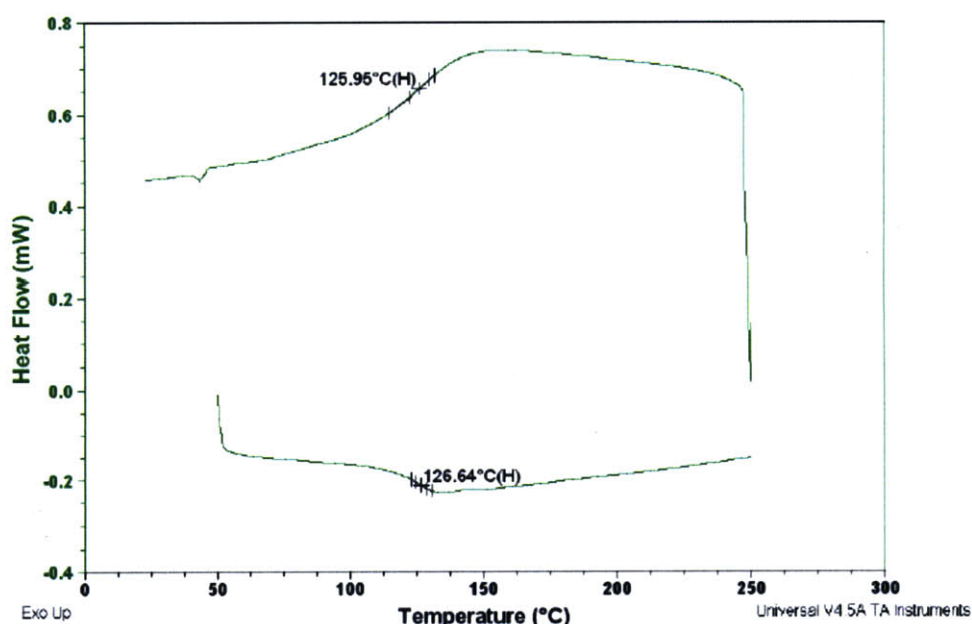


Figure 4: DSC scan of $\text{As}_{25}\text{S}_{75}$ glass. The top and bottom curves are cooling and heating curves respectively. The glass transition temperature is defined as the inflection point on the curves.

The fabrication methodology used in this work sets some of additional requirements on the glass. The glass should have repeatable composition, be a single-phase, and be compatible with the thermal evaporation process. To ensure that the glass meets these criteria, three analysis techniques have been employed: differential scanning calorimetry (DSC), thermal-gravitational analysis (TGA), and electron microprobe composition analysis. DSC (TA instruments, Q1000) directly measures a material's glass

transition temperature (T_g), indirectly measures a material composition and can help determine the phase uniformity in a sample. DSC scans of numerous glass batches have shown a single and predictable glass transition temperature. The single glass transition temperature is evidence of a single phase, while the repeatable glass transition temperature is evidence of a repeatable glass composition. Previous experience drawing PBG fibers suggests that a glass with a T_g of 120 would co-draw with polycarbonate.

TGA (TA instruments, Q50) can be used to measure the phase uniformity of the synthesized bulk glass and to simulate the film deposition process. During a TGA scan, a sample's change in weight is measured versus temperature. Samples of the $As_{25}S_{75}$ constantly have shown continuous changes in sample weight that have a single peak. This additional data supports that the glass has a single phase. A single phase is critical for ensuring that the thermally evaporated films will have a predictable and repeatable composition. Phase separation can also lead to spatial modulations in the glasses index of refraction, which have the potential to scatter light.

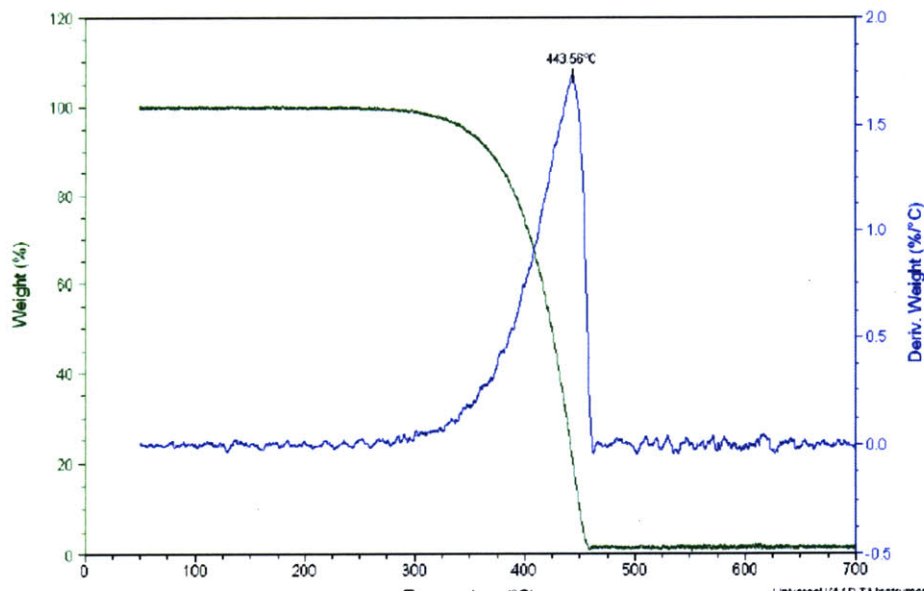


Figure 5: Sample TGA scan of $As_{25}S_{75}$. The weight % and its derivative with temperature are continuous suggesting a single-phase material

The electron microprobe can be used to directly and precisely measure the composition of the bulk glass and the deposited film. The electron microprobe (JEOL JXA-733) uses X-Ray emission spectroscopy to measure compositions to an accuracy of up to 10 parts per million. Microprobe measurements have confirmed that the glass composition synthesized for this thesis consistently has had a composition of $\text{As}_{25}\text{S}_{75}$ (+- 0.5 mol %).

II.C Optical Constants

Accurate measurements of materials optical constants are critical input for optimizing the design of PBG fibers and for simulating their transmission properties. For materials excited in the linear regime, the relevant optical constants are the real (n) and imaginary parts (k) of the index of refraction ($N = n + ik$). When a material is excited by electro-magnetic radiation, the electrons oscillate forming an electronic dipole, which will dampen the amplitude of and induce a phase-shift on the excitation wave. The real portion of the refractive index is the ratio of the speed of light in a medium to the speed of light in vacuum ($c = v_m / n$) and the imaginary part is the amount of energy dissipated in the material.

Spectroscopic ellipsometry is a self-referencing, non-contact technique for measuring both the real and imaginary portions of a materials' refractive index. The technique works by measuring the relative reflection of TE and TM polarized light off of a sample as a function of wavelength. The measured ellipsometer parameters can then be fit to an appropriate model using a regression analysis. The details of the measurement technique can be found in reference 20.

Although ellipsometry can be used to measure the imaginary part of a materials index of refraction, it is a relative technique, which leads to significant uncertainty in the measurement. In practice, ellipsometry often can be most easily performed on a thin film ($<1\mu\text{m}$) evaporated on a highly absorbing substrate, such as a silicon wafer. This sample preparation allows for a strong signal from both the light reflected at the surface of the sample and at interface between the film and the substrate, which is critical for obtaining accurate data for modeling the real part of the refractive index. However, since for even highly absorbing materials only a small fraction of the light will be absorbed in a $<1\mu\text{m}$ film, the measurement tends to be a poor approximation of k .

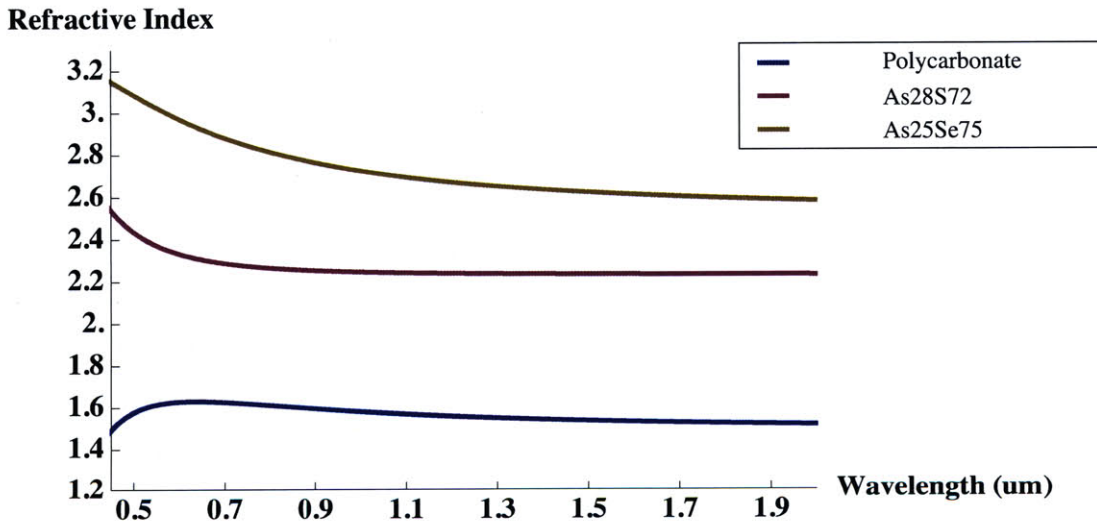


Figure 6: Ellipsometry measurements of the real portion of the refractive index of materials used for fabricating PBG fibers in this thesis

The cutback measurement is generally a more accurate technique for determining k . In a cutback measurement, the absorption of samples with different thicknesses are measured directly in transmission using a light source and detector. The use of multiple sample thicknesses allows for the removal of the uncertainty caused by Fresnel reflections by dividing the signal measured at the detector by the sample thickness. This

calculation gives the materials extinction coefficient (α), which can then used to

determine k, using the relation, $\alpha = \frac{4\pi}{\lambda} k$ (Figure 3, Figure 16).

III Fiber Fabrication

III.A Glass Synthesis

The fiber fabrication process requires that the chalcogenide glass has a repeatable composition, is a single phase and is compatible with the thermal evaporation process. Moreover, we needed to be able to synthesize the glass in quantities sufficient for our experimental needs. To meet these criteria, we employ the commonly used melt-quench technique. In the melt-quench technique, the glass precursors, typically raw elements are loaded into a quartz ampoule. The ampoule is then evacuated using a vacuum pump and sealed with a torch. The charge is then heated to the synthesis temperature and typically rocked and left to homogenize from 12hrs to a couple of days. The glass is then quickly quenched from the melt to freeze it in the glassy state.

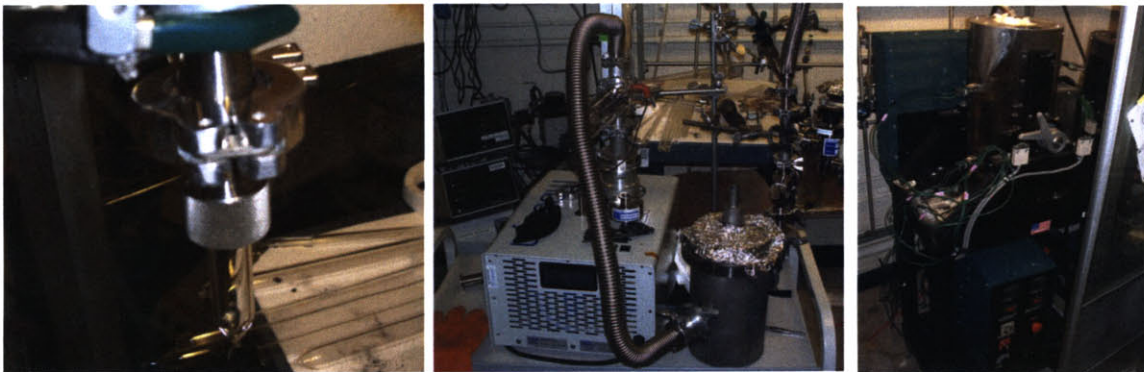


Figure 7: Glass synthesis line; “Quick” coupler to attach the quartz ampoule to the metal vacuum system using an o-ring seal (left), vacuum system including a oil-less turbo-pump capable of $<10^{-6}$ torr (center), and rocking furnace for homogenizing the melt (right).

$As_{25}S_{75}$ is not a commercially available glass composition, which necessitated an investigation into how to properly synthesize the material in relatively large batches (~200 gr.), in order to limit the time devoted to glass synthesis to an acceptable level.

$As_{25}S_{75}$ has a significantly higher vapor pressure than glasses that we have had previous

experience with in the lab. The high vapor and large mass of the charge greatly increases the probability of the quartz ampoule failing during glass synthesis. These destructive failures have the potential to damage expensive synthesis furnaces and are in fact the primary reason that these glasses could not be purchased commercially.

The solution to this problem is three-fold. First, a soaking step at an intermediate temperature (425 °C) for a few hours can be used to react all of the sulfur with the arsenic, before raising the melt to the homogenization temperature (700 °C). This greatly decreases the maximum vapor pressure in ampoule. Second, the strength of the reaction vessel can be increased by using custom well annealed, extra thick-walled, quartz ampoules. Finally, extra precaution is needed when sealing the ampoules to ensure that no singularities, such as induced stresses, thin-walls or sharp angles are introduced. Using this modified methodology, batches of $\text{As}_{25}\text{S}_{75}$ exceeding 200 grams can be synthesized without ampoule failures.

III.B Film deposition

Glass/Polymer bilayers were obtained using a custom roll-to-roll thermal evaporator (Figure 8). During the deposition, the polymer web passes over two sets of evaporator boats, allowing glass to be deposited independently on either side of the film. In order to minimize the penetration depth of the HE_{11} mode into the bilayer structure and coupling to surface states, the glass was deposited at 1/3 of a full glass layer thickness on the inner surface and 2/3 at the outer layer [16]. Electron microprobe analysis (JEOL JXA-733) showed that the arsenic content increases during the evaporation from $\text{As}_{25}\text{S}_{75}$ (+0.5 mol %) to $\text{As}_{28}\text{S}_{72}$ (+1.0 mol %). This is not surprising, since the glass

decomposes from the melt into an arsenic rich vapor ($\text{As}_{25}\text{S}_{75} \rightarrow \text{As}_4\text{S}_4 + \text{S}_2$ [14]) and sulfur gas, which can be preferentially pulled from the chamber.

The operation of the evaporator is fairly complex and a significant effort was needed to modify both the evaporator and deposition procedure to successfully deposit $\text{As}_{25}\text{S}_{75}$. $\text{As}_{25}\text{S}_{75}$ has a high vapor pressure that makes it difficult to maintain a sufficient background pressure, leading to vacuum failures. In addition, the vapor pressure also causes large particles to “jump” from the melt. When these macro-particles hit the film, they simply cause a local defect onto the film. However, when they hit the piezo-electric crystals that monitor the deposition rate, they effectively add a large mass to the surface, greatly decreasing the life of the crystals or causing a crystal failure. These occurrences are especially problematic for $\text{As}_{25}\text{S}_{75}$, since it has a high stiffness that already reduces crystal life. A crystal failure of simply any one of the eight crystals in the system effectively cuts the feedback in the deposition control loop, leading any film deposited after the failure to not have a uniform thickness. Either a crystal or vacuum failure will necessitate the termination of the deposition run, effectively eliminating economies of scale associated with a roll-to-roll deposition system.

Over the course of this thesis, the deposition chamber was modified to minimize the demands on the crystal monitors. Longer shutters were fabricated to shield the crystals during preconditioning of the deposition sources to prevent macro-particles from hitting the crystals, before the source could be homogenized into a melt. The process parameters of the deposition, specifically source’s preconditioning power and time, were also empirically optimized to exercise improved control over the source. This optimization helped prevent both vacuum failures and premature failure of the crystals.

The temperature of the monitor crystals was also increased to allow the deposited film on the crystals to better relieve the induced stress. Finally, the deposition rate was also decreased, which better accommodated the induced stress and allowed the diffusion pump to maintain a sufficient vacuum, even during spikes in the deposition rate.

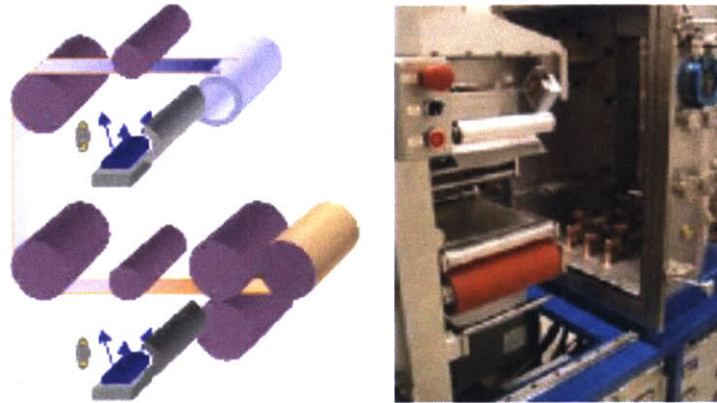


Figure 8: Schematic (left) and photograph (right) of the roll-to-roll deposition chamber (left) taken from ref. 20

These modifications allowed for the deposition of a material that was both more volatile and stiff at a greater thickness than previous experiments. This development was critical for effectively and efficiently fabricating bilayer films. Thickness measurements of these deposited film show that these depositions are also uniform along both the width and the length of the film.

III.C Preform fabrication

Once a uniform polymer-glass film has been fabricated, the theoretical considerations of the preform fabrication process are relatively straightforward. The glass-polymer film is carefully rolled onto a Teflon mandrel to form 15 to 30 periodic bilayers. Additional polymer “cladding” films are then wrapped around the “core” layers to provide mechanical support. Tightly rolled films are then heated under vacuum or

consolidated to form a solid preform to be drawn into hundreds of meter to kilometers of fiber.

During this thesis it became clear that the core-size of the fiber would need to be reduced to improve the transmission properties of the fiber, most specifically its modal content and transmission loss. From a fabrication standpoint, reducing the fiber's core diameter adds additional challenges to preform fabrication. There are two ways to reduce the fiber's core size while maintaining a normalized shrink-down ratio (NS), the ratio between the inner and outer diameter of the fiber with respect to the preform, of 1; using thicker films, effectively increasing the draw ratio or reducing the diameter of the mandrel. Both of these methods increase the mechanical demand on the bilayers films. Reducing the diameter of the mandrel effectively increases the radius of curvature and therefore the strain in the glass layer of the bilayer film. Moreover, increasing the bilayer thickness increases the induced stress in the glass film, since the increased thickness constrains the film's pathway for strain relief. Both mechanisms lead to cracking in the glass layers, delamination and defects in the resultant fiber.

By altering the deposition process parameters, such as deposition rate and temperature at the substrate (polymer), it is possible that stress in the film could be reduced, since amorphous films are not subject to an epitaxial constraint. Nonetheless, chalcogenide glasses, especially $As_{25}S_{75}$, are brittle, so it is unclear how much could be gained through optimization of these parameters. As a result, reduction of the fiber core was done through empirically optimizing the bilayer thickness and the mandrel size. Through practice and a set of custom preform rolling tools, it became possible to produce preforms for fibers with core diameters less than 60 microns (40 wavelengths) at 1.55

microns free of rolling defects. This core-size is sufficient to obtain fibers with the transmission properties outlined as the goal of this work.

Controlling particle contamination was also a key step towards reducing fiber losses. Dust particles can act as sources of scatterers and can create small voids in the fiber bilayers. To minimize contamination, a materials handling protocol was introduced. Rather than engaging in a costly renovation of our lab to clean room standards, a process was developed to take advantage of a class 100 laminar-flow hood. During the fabrication process, the surfaces of the constituent films are exposed only inside the laminar flow hood, except for during the deposition process. A new method was also introduced for cleaning the polymer sheets using a roller that imbeds particles in its surface as it passes over the film. During each pass the roller removes 97% of the particles on the surface of the film. By passing the roller multiple times over the film, we can reduce the particles on the film significantly. This technique was shown to be more effective than cleaning the films with clean room wipes and a solvent such as isopropanol.

III.D Fiber Drawing: Optimizing Draw Parameters

The ability to correlate process parameters to control parameters is critical for developing any fabrication process. Fiber draws for PBG fibers have three process parameters; furnace temperature, capstan speed and pressure applied to the preform's core. The behavior of the rest of the system has already been determined through materials selection and processing. Exercising precise control over the draw parameters is critical for maintaining tight control over the fiber's geometry over meters of fiber. During this work, three control parameters were of particular importance: the fiber's

outer diameter, NS and the fiber’s reflection and transmission bandgaps. In this section we will show how controlling each of the parameters has led to a significant improvement in performances of the Bragg fibers.

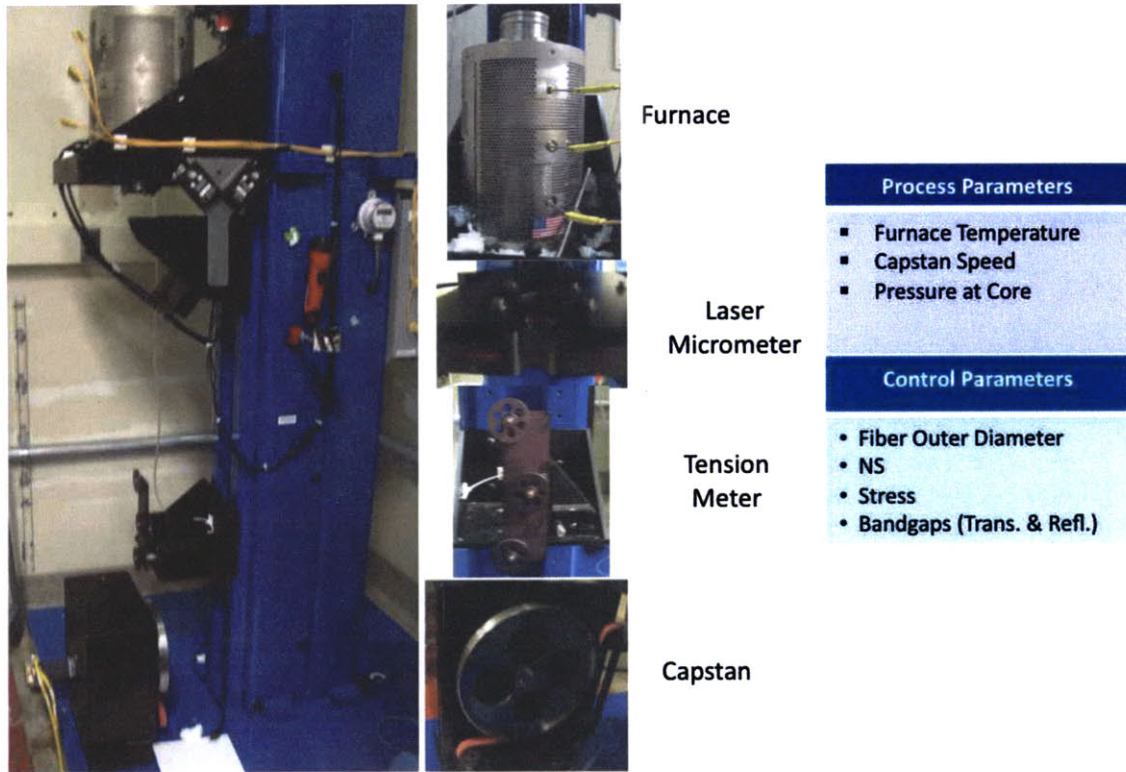


Figure 9: Photographs of the fiber draw tower with enlarged images of the key elements (left), process and control parameters for the fiber drawing process (right).

III.D.1 Controlling the Fiber’s Outer Diameter and Stress

During the fiber draw, a laser micrometer continuously measures the outer diameter of the fiber. This information is then used to calculate additional control parameters, such as the average stress in the fiber and the draw ratio, and to gain additional insight into the fiber draw process. The stress in the fiber is calculated by dividing the tension in the fiber, measured in the tension meter, by the fiber’s cross-sectional area of the fiber, calculated from the fiber’s outer diameter. The operator can use this information to monitor a number of fiber characteristics. Additionally, this data

can also be used as an direct measure of defects along the fiber and an indirect indicator of a fiber's transmission properties such as bandwidth.

Assuming a NS of 1 and a defect free fiber, the draw ratio will determine the bilayers' thickness in the resultant fiber. In this case, any variation in the fiber outer diameter will also be indicative of a modulation in the bilayers' thickness, which will cause a wavelength shift in the photonic bandgap. The net result is that the bandwidth of the fiber will be reduced proportionally to variation in the fibers outer diameter.

Outer diameter fluctuations can also be indicative of various forms of defects in the fiber. Such defects can include contamination particles, molecular inclusions from non-uniformities in polymer molecular weights, crystallizations, and air bubbles. These defects can perturb the fiber core by changing the bilayers thicknesses, pinching or pushing the fiber core and scattering light.

Clearly, variations in the fiber's outer diameter are undesirable. Two main sources for the diameter fluctuations were found to be continuously problematic. The first are the air-void line defects that result from the rolling of successive cladding sheets to form a preform. Each new sheet can potentially produce a linear void down the length of the fiber that can subsequently be expanded when the preform is pressurized during the drawing process. This pressurized line defects will then break-up, during the fiber draw. Improved preform consolidation and sealing of these voids with a high-temperature silicone adhesive has mitigated this problem.

We also observed that drawing instabilities were dependent on the type and purity of polycarbonate resin used for the core sheet and the cladding substrate. Polycarbonate is a widely used material with resins optimized for a number of different applications.

Initially, we had selected a branched polycarbonate resin (Lexan 151), since its high melt-strength enables it to be extruded to a tighter thickness tolerance. After significant experimentation with this polymer over a range of draw temperatures, the fibers consistently had regular outer diameter fluctuations at a length scale less than would be acceptable for a fiber device. During draws of polymer only preforms, it was observed empirically that this resin was highly resistant to flow and had a strong “elastic” component to its viscous flow. A literature search suggested that this can be a fundamental property of branched polymers [24]. It was then reasoned that moving to a linear resin with an increase mass flow rate, would improve the fiber’s outer diameter stability. Experiments drawing a linear polycarbonate resin (Lexan 104) verified this hypothesis. The standard deviation of the fiber’s outer diameter is a good indicator of draw stability. An example plot can be seen in Figure 10. The standard deviation of the fiber’s outer diameter is calculated 1.5 meters before and after a given position along the fiber. Therefore, each point can be seen as representing the standard deviation over a three-meter section of fiber. Over this length scale, the standard deviation has been reduced to less than a 1%, which is significant improvement over previous fibers, such as those made using the branched resin that regularly had diameter fluctuation of 5-10%.

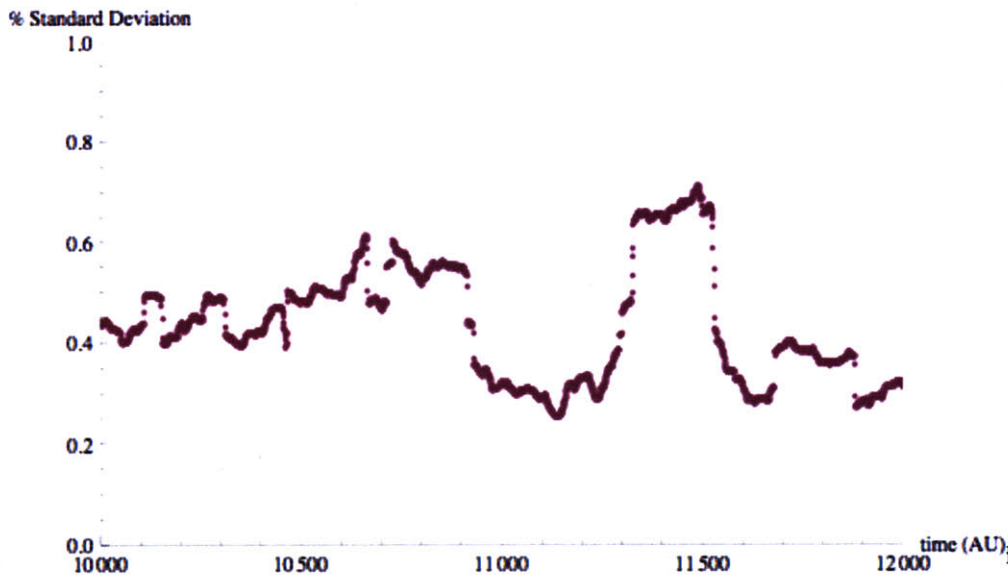


Figure 10 is a running calculation of the standard deviation of three-meter sections of fiber over a forty-meter period

III.D.2 Controlling the NS Ratio

A consequence of reducing the fiber's core diameter to $60\mu\text{m}$ is that surface energy begins to have an increased effect on the drawing process. As the radius of curvature increases at the fiber core, the surface energy of the bilayers drives the core to collapse. To counteract the surface energy effects, the core of the fiber can be pressurized. Pressure can be a difficult process parameter to optimize, since its effect on the fiber's core diameter is highly dependent on the preform's viscosity, the preform's inner diameter, and the number of bilayers in the preform. As a result, it has taken time to optimize the fiber drawing in this parameter space.

If the NS is less than 1, the bilayers will be thicker than designed and the bandgap will shift to longer wavelengths. If NS greater than 1, the bilayers will be thinner and the bandgap will shift to shorter wavelengths. Moreover when the NS deviates from 1, the width of the bandgap will narrow and the fiber's transmission spectrum will be reduced, since the bilayers will deviate from a periodic thickness profile (bilayer chirp).

This effect can be understood through a conservation of cross-sectional area argument from the preform to the fiber level.

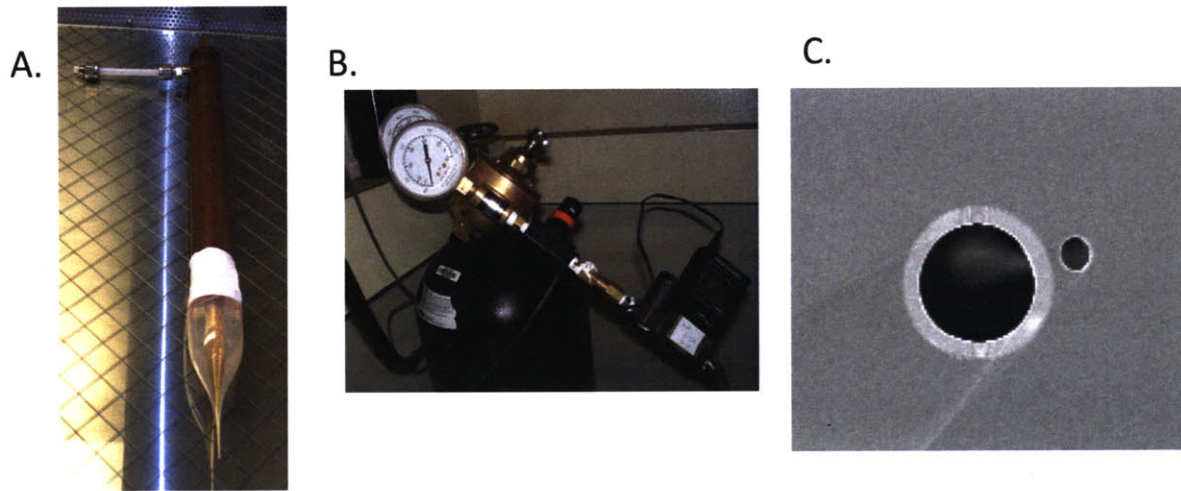


Figure 11: Preform sealed to preform holder with high-temperature silicon adhesive, covered with Teflon tape (A). Mass-flow, pressure controller (B). The void adjacent to the fiber core is defect from not properly sealing line defects in the preform (C).

The NS ratio of the fiber is measured throughout the draw using a microscope with a reticule as a reference. A mass-flow pressure controller is used to adjust the applied pressure to make small changes in the NS ratio. Over the work of this thesis, the requisite knowledge for empirical determination of this process parameter has been gained, such that the NS can now routinely be maintained close to one throughout a fiber draw.

III.D.3 Monitoring the Photonic Bandgap

In addition to exercising precise control of the fiber's geometry during the draw, it is also critical to monitor the fiber's photonic bandgap. Despite careful attempts to control the geometry of the photonic bandgap structure throughout each of the fabrication steps, the resultant fiber will inevitably deviate from an ideal structure. Variations in bilayer thickness and the resultant optical thickness necessitate adjustments of the draw

ratio throughout the draw to ensure that the fiber has the correct bandgap. Moreover, careful monitoring of the transmission and reflection bandgaps during the draw enables the efficient identification of fibers suitable for further post-draw analysis.

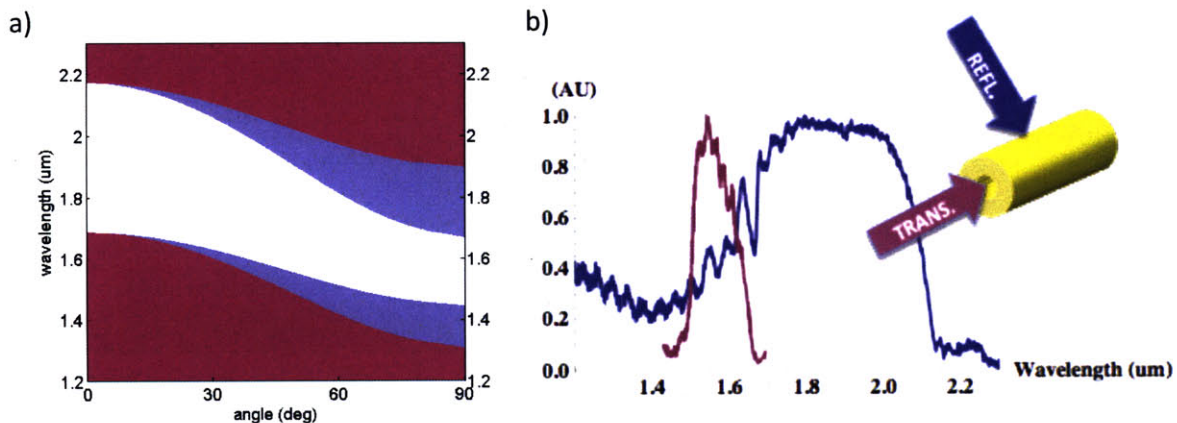


Figure 12: (a) Simulated band diagram for an ideal PBG structure of $As_{25}S_{75}$ and polycarbonate with a fundamental bandgap centered at $1.55\mu m$. Regions with propagating modes are shaded (blue for TM, red for TE and purple for both) (b) Measured transmission ($\theta=90$) and reflection ($\theta=0$) bandgaps for the PBG fiber described in this paper.

During fiber drawing, the PBG is monitored in two ways; first a FTIR microscope measures reflections normal to the PBG structure and, second, a spectrometer measures the transmission spectrum at grazing incidence. Together, these two techniques form a complimentary set of measurements that can be used to gain significant insight into both the structure and transmission properties of a fiber sample. The importance of measuring the transmission spectrum of a fiber is perhaps more straightforward and will be discussed first.

Certainly, it is critical for the draw operator to know the position of the transmission bandgap, so that they can make small adjustments to the position of the center of a fiber's bandgap. Previously, the external port of a FTIR was used for transmission measurements. The thermal light source of a FTIR is poorly collimated and therefore cannot be strongly focused. When core of the fiber was reduced to from $160\mu m$ to $60\mu m$ the spot-size of the FTIR could not be further reduced. Therefore, the signal to

noise ratio (SNR) was reduced by an order of magnitude, since the power at the input of the fiber scales with the square of the core size. The resultant SNR was too low to be used for the 60 μ m core fibers fabricated in this work.



Figure 13: Schematic of transmission bandgap measurements during the fiber draw

Fortunately, highly sensitive near-infrared spectrometers have been recently commercialized. The spectrometer (Photon Control, SPM-002-NIR1700), used in this work, is fiber coupled and can measure a spectral response from 900-1700nm in a parallel, using a diffraction grating and an array of InGaAs detectors. When used with a fiber coupled white light source (broadband thermal source), the spectrometer enables the measurement of a fiber sample's transmission bandgap in less than a second with only a couple of minutes dedicated to coupling the output of the sample fiber to the spectrometer. This real time feedback during the draw allows the draw operator to make small adjustments to process parameters to optimize both the center of the bandgap and its spectral width.

The transmission bandgap measurement essentially integrates the properties of PBG structure over the circumference of the fiber's inner diameter and along the length of the fiber sample. Therefore, the interpretation of the transmission measurement relies on the PBG structure to be uniform over 2π -radians, down the entire length of the sample. This measurement is powerful, since it gives insight into the net properties of the fiber's PBG, but it comes at the expense of averaging local features.

Although the reflection bandgap is an indirect measurement of the fiber's transmission properties, it can give additional access to information about the PBG structure that the transmission measurement often obscures. Besides exhibiting a PBG, high-index contrast, well-ordered periodic films also have interference fringes that decay away from the primary bandgap (Figure 12). These fringes are an indication of the extent of the film's periodicity and are usually obscured in transmission.

The reflection PBG itself also contains important information about the fiber's structure. If the bilayer structure is chirped, both the transmission and reflection bandgaps will narrow. However, narrowing of the transmission bandgap can also be due to fluctuations in the fiber's outer diameter along length of the sample. Since the reflection measurement gives information at one location in the fiber, rather than integrating a large area, it can help determine if the narrowing is due to diameter fluctuations or chirping of the bilayers. This information is critical, since chirp is best corrected for with a pressure adjustment, while outer diameter variation may be best corrected by changing the furnace temperature.

Therefore, in order to take advantage of the significance of the transmission and reflection measurements, they should be analyzed in the context of the other draw parameters. The net result is a significantly higher yield of fibers with the correct bandgap and an increased ability to pre-screen which sections of the draw are good candidates for efficient analysis in the optics lab.

IV Fiber Analysis and Transmission Measurements

IV.A Draw Slides and Pre-Screening Fibers

During the fiber draw, the process and control parameters are measured and logged. Since much of this data is continuously collected, the data quickly can become overwhelming. Organizing this data in a manner that can then be further analyzed after the draw is critical. One methodology is to create draw slides where the relevant process data can be plotted next to the fiber's geometry and bandgap measurements. Figure 14 shows an example of such a draw slide.

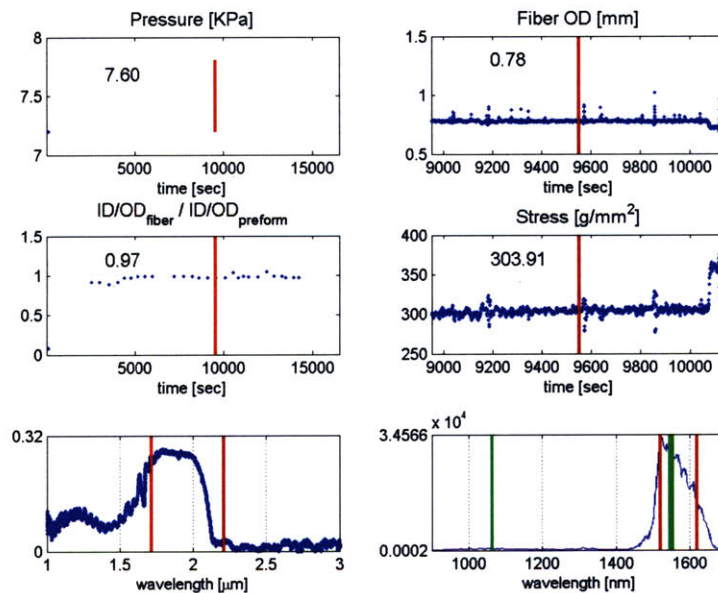


Figure 14: Sample Draw slide. The red and green lines on the slides show relevant positions of the plots such as position along the fiber, positions of the bandgap, relevant laser lines etc.

A typical fiber draw generates well over a kilometer of fiber. In a laboratory environment, it is impractical to characterize more than a small percentage of the fiber draw. However, once the draw slides are generated, it quickly becomes clear which fibers will be interesting for further analysis. Additionally, the draw slides can be used to

correlate process parameters such as temperature, which largely determines the stress in the fiber to phenomenon such as outer diameter instabilities.

IV.B Fiber Cross-sectional Images and Analysis

Unlike the previously discussed techniques, fiber cross-sectional imaging allows for direct access into the fiber's structure. Fiber defects such as bubbles, inclusions, delamination and surface roughness can be clearly identified under scanning electron microscopy (SEM). Image analysis software can also be used to measure quantitatively the fiber's geometry, such as its inner diameter, outer diameter and bilayer thicknesses. SEM images taken at a high magnification also can be analyzed using a spatial Fourier transform to give a quantitative measurement of the bilayers' thickness distribution. This information in conjunction with the draw slides and the optical measurements, discussed in next three sections, forms a robust set of data that enables the correlation of the fiber's structure to the processing methodology and the fiber's transmission properties.

Cross-sectional fiber samples were prepared using an argon ion-polisher (JEOL, SM-Z04004T). SEM (JEOL 6060) images show that the preform's geometry is maintained through the fiber drawing process. The 760-micron outer diameter fiber has a NS of 1 and a 60-micron core (40λ at $1.5\mu\text{m}$). The images show smooth interfaces between the glass and polymer layers. Fourier analysis on the SEM image of the 22 glass-polymer bilayers reveals a sharp peak at 521nm, agreeing strongly with our simulations. There is a tight distribution in the bilayer thickness with a full-width at half-maximum (FWHM) of 27nm, which is below the resolution of the SEM image.

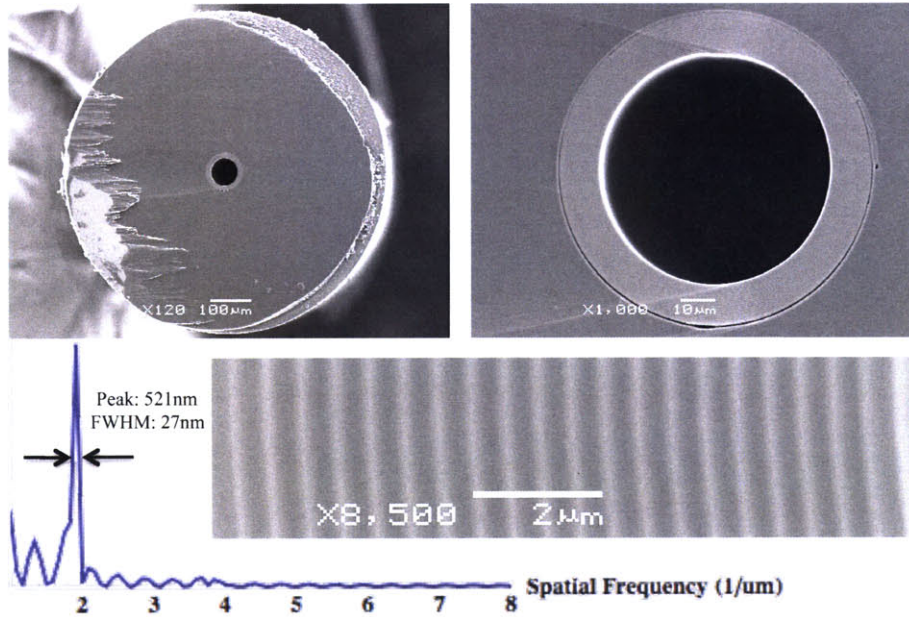


Figure 15: Cross-sectional SEM images of a PBG fiber with a 60 μm -core, a 760 μm outer diameter and Fourier analysis of the glass-polymer bilayers

IV.C Propagation Loss Measurements

Propagation loss is a key quantitative measure of fiber performance. Certainly, we would like to minimize this quantity in order to maximize the power transmitted through the fiber.

Propagation loss measurements were performed using the cutback method. The output of a single mode fiber coupled to a frequency-swept laser source from 1520nm-1620nm (Ando) provided a linear polarized Gaussian beam for the measurement. A spherical lens coupled the beam preferentially into the HE_{11} mode; the fiber's lowest order linearly polarized mode. A 2-meter section of fiber was held straight and cutback five times to 1-meter. Over the 100nm bandwidth of the laser, the propagation losses are from 2-3 dB/m, with a minimum loss of less than 2dB/m at 1560nm. The propagation losses are a significant improvement over previously published work of 5.5 dB/m for a

160 μm -core fiber [9]. Absorption and scattering losses scale as $1/R^3$, corresponding to a 52x improvement compared to the fiber in this work [17].

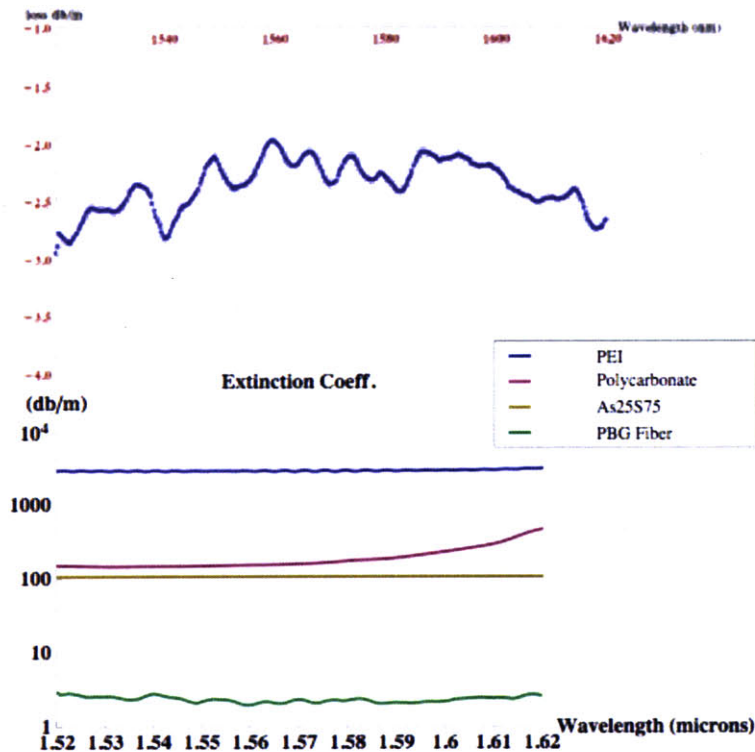


Figure 16: Cutback Measurement of PC/As₂₅S₇₅ PBG fiber (Top). Plot of the extinction coefficients of material used to fabricate the PBG fiber and the fiber's losses in the wavelength range of the frequency swept laser.

Despite these improvements, the fiber still exhibits propagation losses for the HE₁₁ mode that are two orders of magnitude greater than simulations that account for materials' absorption and the finite number of layers in the photonic crystal. An integrating sphere and detector were used to measure the power radiating from the fiber as the sphere was moved along the fiber. The radiation losses matched the propagation losses measured using the cutback technique. Therefore, scattering mechanisms such as interface roughness (air/core, bilayer) and inclusions (dust, phase separation) are likely limiting fiber performance and will be subject to further investigation.

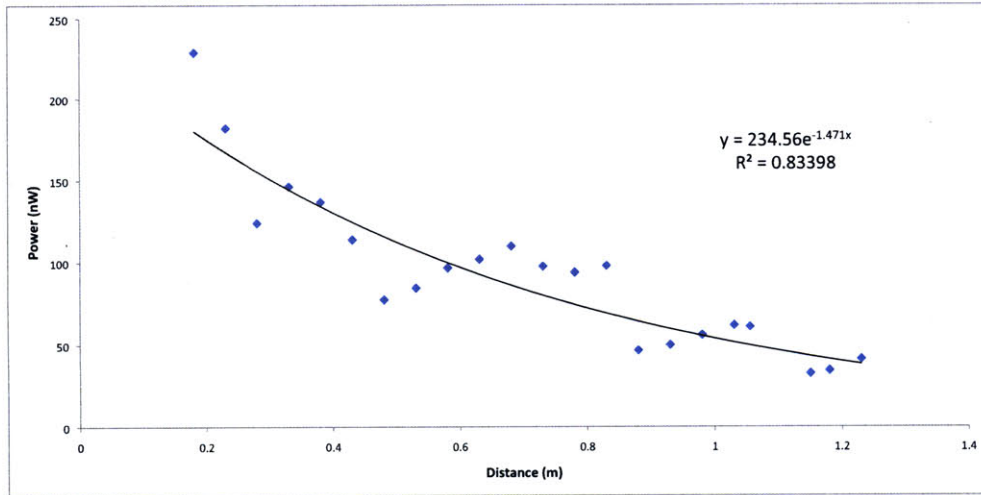


Figure 17: Radiation collected along the fiber as a function of position. The R^2 fit parameter shows that the fit is in good agreement with an exponential decay

IV.D Modal Analysis

The modal content of the fiber's output was analyzed using a mode decomposition algorithm developed previously in our group [15]. Reducing the fiber's core-size limits modal coupling, since the spacing between modes scale as $1/R^2$ [5]. Unlike previously demonstrated NIR fibers with larger cores, the modal content at the output of these fibers is over 97% HE_{11} . Since the HE_{11} mode overlaps strongly with a Gaussian beam, the fiber's output can be highly focused for applications where power density is critical. Another consequence of the increased mode spacing is that no additional bending losses were observed down to radii sufficient to damage the fiber mechanically (~ 2 cm), when careful attention is paid to maintain the input coupling.

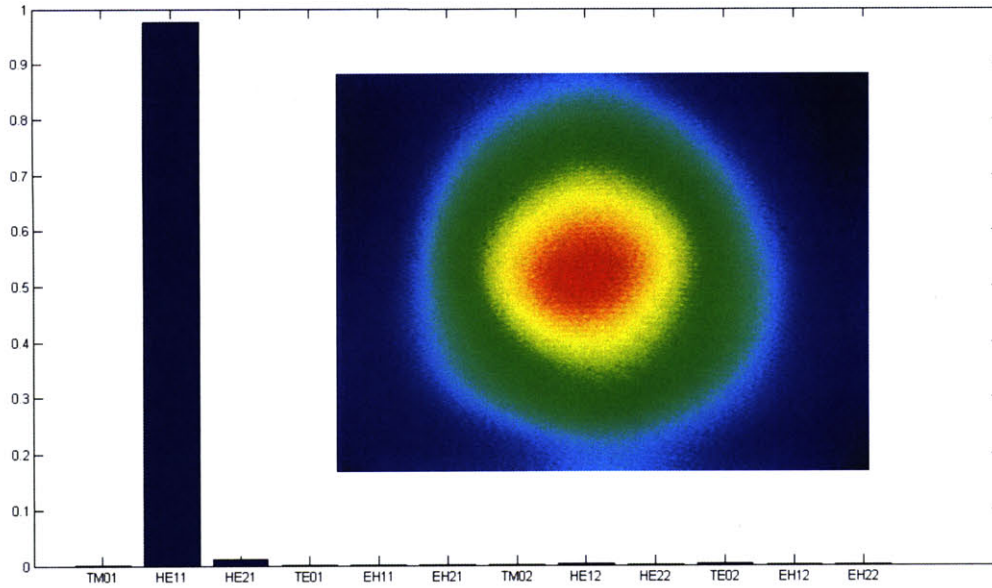


Figure 18: Far-Field intensity distribution at the output of the PBG fiber after 1-meter, excited at 1.55 μ m and the proportional modal content of the first 12 modes as determined by the modal-decomposition algorithm

IV.E Power Handling Measurements

Power handling measurements were performed using a laser source delivering 1-ps, 50 μ j pulses at 100kHz centered at 1.552 μ m (Raydiance Inc.). The output of the laser was coupled to the fiber using a spherical lens. No additional beam shaping or end-facet protection, such as a ferrule or pinhole, was used. The input coupling efficiency was about 90% at low powers. The output of the PBG fiber was measured using an optical spectrum analyzer, an autocorrelator and power meter. A half-wave plate and polarizing beam-splitter were used to slowly increase the power coupled to the fiber until failure. Failure occurred at the end-facet at 12.7 μ j corresponding to a peak power of 11.4 MW and an average power of 1.14W. The HE₁₁ mode of a 60 μ m core fiber has a mode field diameter of 35 μ m, corresponding to a power density of 1.2 TW/cm² in the fiber core. As

the input power increased, there was no observable change in the pulse width or spectrum at the output of the fiber, suggesting non-linearities are not significant (fig. 4b).

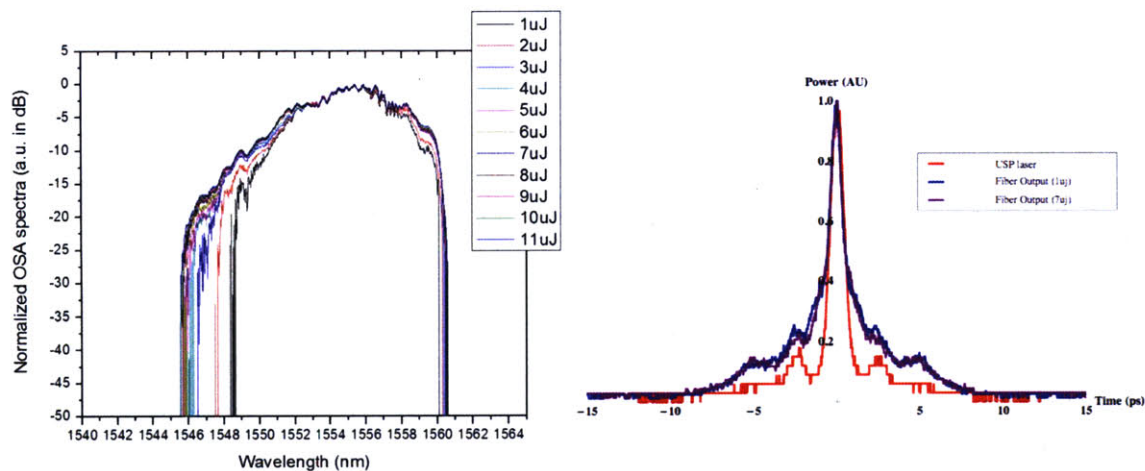


Figure 19: Fiber output spectrum as a function of input power (left), measured using an optical spectrum analyzer (OSA, left). Temporal trace of the fiber output as a function of input power using an autocorrelator (right).

To our knowledge, the highest reported peak-power for air-silica PCF fiber around $1.5\mu\text{m}$ is 2.4 MW at atmosphere, using 110-fs pulses and a $12.7\mu\text{m}$ core fiber [18]. We have not been able to find any studies that have determined the bulk damage threshold for silica at $1.55\mu\text{m}$ for comparison. However, the bulk damage threshold for silica at $1.064\mu\text{m}$ has recently been established to be in the $1.4\text{ TW}/\text{cm}^2$ range for 14-ps pulses [19]. The damage threshold at the air-silica interface is considerably lower unless careful steps have been taken to completely eliminate surface roughness.

V Conclusion and Future Directions

In this thesis, PBG fibers were fabricated in a new materials system, which has enabled the realization of fibers with $60\mu\text{m}$ -cores and propagation losses below 2dB/m . Through preferential coupling, these fibers can be used to transmit pulses with modal profiles approaching a single mode and peak-pulses up to 11.4 MW . Further investigations are required to study and to minimize scattering losses, which currently set the radiation-limited propagation losses for PBG fibers. Improving the input coupling should also increase the coupling efficiency and power-handling limit of the fibers. We believe that this work supports the viability of using polymer-composite PBG fibers to deliver high peak power pulses in the NIR.

VI Appendix: End-Facet Preparation

Not surprisingly, coupling into PBG fibers is highly dependent on the fiber's end-facet preparation. The polymer and glass fibers constituents are engineered to have similar mechanical properties in viscous state. However, at room temperature the glass and polymer behave quite differently mechanically. The glass is extremely brittle, while the polymer is ductile. When a PBG is simply cut with a microtome blade, the bilayer structure will delaminate, blocking the core. This phenomenon lead to an investigation on how to prepare the fiber end-facets for laboratory experiments.

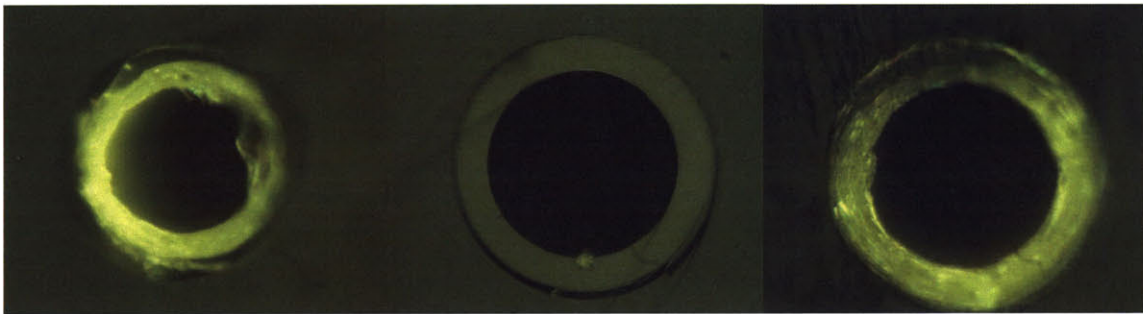


Figure 20: Optical microscope images of fiber-end facet prepared by cutting with a microtome blade (left), prepared with an ion-polisher (center), prepared by injecting water into the fiber core, freezing with liquid nitrogen and cutting with a microtome blade (right).

As demonstrated in the SEM images, ion-polishing is an effective non-mechanical method for end-facet preparation without delamination. Ion-polishing a single end-facet of a 760 μm fiber typically takes at least 12 hours, which is impractical most measurements. In addition, there is some evidence that the technique tends to deposit materials inside the fiber core, which will later cause failures during high-peak power measurements and obscure the fibers modal output, introducing uncertainty to the fiber's modal content.

During this thesis, it was observed that the layers seemed to be delaminating under the compression of the microtome blade. Therefore, it seemed reasonable that mechanically supporting the core with a solid during the cut with a microtome blade could improve the quality of the fiber end-facet. Water-soluble materials with low melting temperatures such as crystal bond were first experimented with. However, it was difficult to remove all of the residual material, since the fiber cores have small diameters and are hydrophobic. The next experiment was to freeze various laboratory solvents in the fiber core with liquid nitrogen. It was observed that the liquid consistently was not getting into the core, or was later displaced by the liquid nitrogen. The solution was to start with ice water and to dip the end-facet vigorously in the liquid and then dip the fiber in liquid nitrogen. Since the water only needs to overcome the latent heat of freezing, it freezes efficiently. The water can then be removed either by gently heating the fiber or placing it in a vacuum chamber.

VII References

- [1] B. Richou, I. Schertz, I. Gobin, and J. Richou, "Delivery of 10-MW Nd:YAG laser pulses by large-core optical fibers: dependence of the laser-intensity profile on beam propagation," *Appl. Opt.* **36**, 1610-1614 (1997).
- [2] Y. Matsuura, K. Hanamoto, S. Sato, and M. Miyagi, "Hollow-fiber delivery of high-power pulsed Nd:YAG laser light," *Opt. Lett.* **23**, 1858–1860 (1998).
- [3] S. Konorov, V. Mitrokhin, A. Fedotov, D. Sidorov-Biryukov, V. Beloglazov, N. Skibina, A. Shcherbakov, E. Wintner, M. Scalora, and A. Zheltikov, "Laser Ablation of Dental Tissues with Picosecond Pulses of 1.06- μm Radiation Transmitted through a Hollow-Core Photonic-Crystal Fiber," *Appl. Opt.* **43**, 2251-2256 (2004).
- [4] NKT Photonics. Data sheet. <http://www.nktp Photonics.com/>, Accessed November 2009.
- [5] S. G. Johnson, M. Ibanescu, M. Skorobogatiy, O. Weisberg, T. D. Engeness, M. Soljacic, S. A. Jacobs, J. D. Joannopoulos, and Y. Fink "Low-loss asymptotically single-mode propagation in large-core OmniGuide fibers," *Opt. Express* **9**, 748-779 (2001)
- [6] P. Yeh, A. Yariv, and E. Marom, "Theory of Bragg fiber," *J. Opt. Soc* **68**, 1196-1201 (1978).
- [7] Y. Fink, J. N. Winn, S. Fan, C. Chen, J. Michel, J. D. Joannopoulos, and E. L. Thomas, "A dielectric omnidirectional reflector," *Science* **282**, 1679-1682 (1998).
- [8] Y. Fink, D.J. Ripin, S. Fan, C. Chen, J.D. Joannopoulos, E.L. Thomas, "Guiding optical light in air using an all- dielectric structure," *J. Lightwave Technol.* **17**, 2039-2041 (1999).
- [9] K. Kuriki, O. Shapira, S. Hart, G. Benoit, Y. Kuriki, J. Viens, M. Bayindir, J. Joannopoulos, and Y. Fink, "Hollow multilayer photonic bandgap fibers for NIR applications," *Opt. Express* **12**, 1510-1517 (2004).
- [10] B. Temelkuran, S. D. Hart, G. Benoit, J. D. Joannopoulos and Y. Fink, "Wavelength-scalable hollow optical fibres with large photonic bandgaps for CO₂ laser transmission," *Nature* **420**, 650-653 (2002).
- [11] T. Engeness, M. Ibanescu, S. Johnson, O. Weisberg, M. Skorobogatiy, S. Jacobs, and Y. Fink, "Dispersion tailoring and compensation by modal interactions in OmniGuide fibers," *Opt. Express* **11**, 1175-1196 (2003)
- [12] O. Shapira, K. Kuriki, N. D. Orf, A.F. Abouraddy, G. Benoit, J.F. Viens, M. M. Brewster, A. Rodriguez, M. Ibanesc, J.D. Joannopoulos, Y. Fink. "Surface-Emitting Fiber Lasers," *Opt. Express* **14**, 3929-3935 (2006)
- [13] E. Bychkov, M. Miloshova, D.L. Price, C.J. Benmore, A. Lorriaux. "Short, intermediate and mesoscopic range order in sulfur-rich binary glasses". *Journal of Non-Crystalline Solids*. Volume 352, Issue 1, 1 January 2006, Pages 63-70.

- [14] Z.U. Borisova, *Glassy Semiconductors*, Plenum, New York, 1981.
- [15] Shapira, O., Abouraddy, A.F., Joannopoulos, J.D., Fink, Y., "Complete modal decomposition for optical waveguides," *Physical Review Letters*, 94, 14, 143902/1-4 (2005).
- [16] V. Nguyen, F. Sanghera, B. Cole, P. Pureza, F.H. Kung, I. D. Aggarwal. "Fabrication of Arsenic Sulfide Optical Fiber with Low Hydrogen Impurities". *J. Am. Ceram. Soc.*, 85 [8] 2056–58 (2002)
- [17] Mendez and Morse. *Specialty Optical fibers handbook*. Elsevier. 2007
- [18] D. G. Ouzounov, F. R. Ahmad, D Müller, N. Venkataraman, M. T. Gallagher, M. G. Thomas, J. Silcox, K. W. Koch, A. L. Gaeta* "Generation of Megawatt Optical Solitons in Hollow-Core Photonic Band-Gap Fibers". *Science*. 1702 (2003); 301
- [19] A. V. Smith, B. T. Do, "Bulk and surface laser damage of silica by picosecond and nanosecond pulses at 1064 nm," *Appl. Opt.* **47**, 4812-4832 (2008)
- [20] G. Benoit. "Tunable micro-cavities in photonic band-gap yarns and optical fibers". Ph. D. Thesis, Department of Materials Science and Engineering. Massachusetts Institute of Technology. Cambridge, MA. 2006
- [21] Joannopoulos J. D., Meade R. D. and Winn J. N. *Photonic Crystals - Molding the flow of Light*. 2nd Edition, Princeton University Press, Princeton, 2008.
- [22] Yeh P. *Optical Waves in Layered Media*. John Wiley & Sons, New York, 1988.
- [23] M. Ibanescu, S. G. Johnson, M. Soljačić, J. D. Joannopoulos, Y. Fink, O. Weisberg, T. D. Engeness, S. A. Jacobs, and M. Skorobogatiy, "Analysis of mode structure in hollow dielectric waveguide fibers," *Physical Review E*, vol. 67, p. 046608, 2003
- [24] D. LeGrand. *Handbook of Polycarbonate Science and Technology*. Marcel Dekker Inc., New York, 2000.